CrystEngComm

Two-Step Route to Size and Shape Controlled Gibbsite Nanoplates and the Crystal Growth Mechanism

Journal:	*CrystEngComm*
Manuscript ID	CE-ART-01-2020-000114.R1
Article Type:	Paper
Date Submitted by the Author:	03-Mar-2020
Complete List of Authors:	Wang, Suyun; Pacific Northwest National Laboratory Zhang, Xin; Pacific Northwest National Laboratory, Graham, Trent; Pacific Northwest National Laboratory Zhang, Hailin; Pacific Northwest National Laboratory Pearce, Carolyn; Pacific Northwest National Laboratory Wang, Zheming; Pacific Northwest National Laboratory, Clark, Sue; Pacific Northwest National Laboratory, Chief Scientist & Technology Officer Jiang, Wei; Nanjing University of Science and Technology, Rosso, Kevin; Pacific Northwest National Laboratory, Physical Sciences Division

Two-Step Route to Size and Shape Controlled Gibbsite Nanoplates and the Crystal Growth Mechanism

Suyun Wang[†, ‡], Xin Zhang[†], Trent R. Graham[†], Hailin Zhang[†], Carolyn I. Pearce[§], Zheming Wang[†], Sue B. Clark[§, ‖], Wei Jiang [*‡] and Kevin M. Rosso[*†]*

[†] Physical & Computational Sciences Directorate, Pacific Northwest National Laboratory, Richland, Washington 99354, USA

[‡] School of Chemical Engineering, Nanjing University of Science and Technology, Nanjing 210094, China

[§] Energy & Environment Directorate, Pacific Northwest National Laboratory, Richland, WA, USA

[‖] The Voiland School of Chemical and Biological Engineering, Washington State University, Pullman, Washington, USA

Abstract:

Mastery of gibbsite (α-$Al(OH)_3$) nucleation and crystal growth is significant in fundamental aluminum chemistry and also beneficial for industrial applications and the remediation of nuclear waste. Herein, we developed an additive-free two-step route to size and morphology controlled synthesis of gibbsite nanoplates. Independent temperature manipulation of nucleation and crystal growth regimes was used to control the efficacy and yield of the process, producing gibbsite nanoplates with tunable morphologies and sizes. We achieve morphologies ranging from hexagon, pseudo hexagon, truncated triangle to rhombic, and average basal plane diameters from 120 to 850 nm, with thicknesses between 5 and 45 nm. Analysis of gibbsite structure, size and morphology with techniques including powder X-ray diffraction (p-XRD), ^{27}Al magic

angle spinning nuclear magnetic resonance spectroscopy (MAS NMR), scanning electron microscopy (SEM), and atomic force microscopy (AFM) provided key details on the nucleation and crystal growth mechanisms. The results indicate the temperature of the nucleation aging step is the most important factor controlling the final particle size. Particularly small nanoplates were obtained with a low nucleation aging temperature followed by high crystal growth temperature, suggesting that gibbsite growth can be approximated via a LaMer-type burst nucleation and crystal growth mechanism. Scalability was demonstrated by triplicate of 2 L experiments which prepared gibbsite nanoplates of ~200 nm size and with an average yield of ~ 55% after 84 h. Compared to existing techniques, this improved two-step route is cheaper, more efficient and environmentally friendly.

Keywords: Gibbsite; Synthesis; Nucleation and crystal growth; LaMer mechanism; Two-step route

Introduction:

Gibbsite (α-$Al(OH)_3$) is one of the most common mineralogic forms of aluminum in nature and is important to a variety of industries.[1-6] Examples include its use as a sorbent of heavy metals and toxic organics, toothpaste polishing agent, paper manufacturing filler, and as a castable ceramics porogenic agent.[1, 3, 7] Gibbsite is also an important precursor in the preparation of high-quality Al_2O_3 which in turn has uses in catalysis and the production of ceramics, semiconductors, coatings, etc.[5, 8] In addition, gibbsite is a major component in the complex high-level nuclear wastes stored at the Hanford Nuclear Reservation (WA, USA) and at the Savannah River Site (SC, USA).[9-15]

Development of highly precise gibbsite nanomaterials as a model experimental platform for materials research is a pervasive need across many of these areas. Gibbsite has a sheet structure comprised of edge-sharing $Al^{3+}(OH)_6$ octahedra in which close-packed hydroxyl layers are two-thirds occupied. Sheets are bound together along the c-axis via interlayer hydrogen bonding, yielding a pseudohexagonal structure (**Fig. S1**).[2,

[5, 16] Consequently, lab-synthesized gibbsite nanoparticles tend to adopt a hexagonal platelet morphology, which includes two dominant (001) basal surfaces truncated at edges by four equivalent (110) and two equivalent (100) surfaces.[16]

The most common commercial method for large-scale production of gibbsite is the Bayer method, developed by Karl Josef Bayer in 1888, involving digestion, separation, crystallization and washing steps.[17] For modern laboratory grade materials this approach is beset by impurities that lead to uncontrolled properties of the gibbsite product.[18] Park et al. introduced multi-stage acid treatment to obtain higher purity Bayer gibbsite but this still yields a wide particle size distribution ranging from hundreds of nanometers to hundreds of micrometers and various particle shapes such as prisms and hexagons[4, 8, 18-19].

Typically at the sacrifice of high-yields, gaining control of purity, particle shape and size distribution has required more precise laboratory-based methods,[20-29] and recognition of the fact that gibbsite growth is slow and the resulting morphology depends on the chemical reactivity and growth kinetics of individual facets.[3, 16] Such approaches include hydrolysis and polycondensation of organic aluminum alkoxide salts (such as aluminum-iso-propoxide, aluminum ethoxide and aluminum sec-butoxide),[30-31] often resulting in gibbsite nanoplates exhibiting a basal diameter of ca. 160 nm.[30, 32] These syntheses typically are conducted under acidic conditions over the course of several days at room temperature, followed by a hydrothermal process at 80 - 100°C for another several days. Drawbacks include the residual, surface-complexed organics and the low yields (< 30%).[18] Another method, free of organics, entails heating amorphous aluminum hydroxide (AAH) suspensions made by mixing $AlCl_3$ and NaOH solutions at low reaction temperatures (< 60°C). For example, pseudo-hexagonal gibbsite nanoplates with a basal diameter and thickness of 200 and 10 nm, respectively, can be prepared over 9 months.[33] Similarly, 100 nm gibbsite nanoplates result after heating aluminum hydroxide suspension at 50°C for two months, but with low yields.[34]

Temperature is clearly an important master variable; low reaction temperature is a

route to nanosized platelets but at the expense of long reaction times. In our recent work we developed an additive-free method to synthesize gibbsite nanoplates at elevated temperatures between 60-80°C using AAH as the precursor.[16] The gibbsite product was highly uniform euhedral hexagonal nanoplates of diameters ranging from 200 to 400 nm, and a box-behnken design strategy was applied to optimize the yield up to 88%. Smaller particle sizes were obtained at lower temperatures, but this also made it difficult to eliminate residual amorphous nanoparticles. It has been speculated that the main temperature effect on the rate is promotion of agglomeration of crystal nuclei.[16] Higher temperatures are therefore important to exploit both for faster crystal growth rate and reaction completeness, but the challenge that remains is in maintaining a slower rate of nuclei agglomeration that appears to lead to the smaller particle sizes at lower temperatures.

Here, building on our prior work, we report an additive-free two-step route to size and morphology-controlled gibbsite nanoplatelets. The main advance results from independent thermal manipulation of nucleation and crystal growth regimes, leading to substantially more range of controlled properties with shorter reaction times. We introduce an initial aging step at low temperature to slow the nucleation regime, followed by crystal growth at higher temperature to improve the rate and extent of reaction. Notably, we found that the effect of the nucleation aging step propagates through the higher temperature treatment, yielding access to much smaller particle sizes of high quality similar to those synthesized at higher temperatures alone. Gibbsite nanoplates with various morphologies and with a diameter in the range of 120 - 850 nm and thicknesses of 8 - 45 nm are thus demonstrated. We also performed scale-up experiments in 2 L vessels, achieving an average yield of around 55%. Detailed multi-method characterization enabled insights into the nucleation and crystal growth mechanisms of these gibbsite nanoplates, insights that may help in the development of economical size- and facet-optimized nanogibbsite materials for myriad applications.

Experimental Methods

Synthesis of AAH precursor. Synthesis of the AAH was performed according to previous work.[16] Briefly, a homogeneous $Al(NO_3)_3$ aqueous solution was prepared via dissolution of 200 g $Al(NO_3)_3 \cdot 9H_2O$ (≥98%, Sigma-Aldrich) in 2 L deionized (DI) water (18 MΩ·cm), at room temperature. Then, by dropwise addition of 3 M NaOH (≥ 98%, Sigma-Aldrich), the pH of the aqueous solution was adjusted to around 5.0 while stirring. After continuous stirring at room temperature for 1h, precipitates were collected via centrifugation (8600 rpm, 30 min) and washed with deionized water three times to remove residual Na^+ and NO_3^-. Finally, the obtained AAH particles were dispersed into DI water to prepare 0.25 M (based on Al ions) AAH suspensions.

Synthesis of gibbsite nanoplates. The above AAH suspensions were aged at 25℃ for 7 days, 50°C for 3 days, 80°C for 24 hours or 100°C for 10 hours, to prepare the 25, 50, 80, or 100°C aged solutions, denoted as G25, G50, G80, and G100, respectively. The duration of the aging step at different temperatures was determined to be the point at which AAH by visual inspection was dissolved completely and minimal solids were obtained by separation using centrifugation at 8600 rpm for 30 min. This point was designated as the transition between AAH dissolution and the beginning of the crystal growth stage. These aging solutions were then treated at different temperatures for the second step, as detailed in **Scheme 1**. For samples obtained from higher aging temperature and lower growing temperature, we relied on ambient cooling rates to achieve the required temperature decrease (approximately 5 ^oC /min); conversely, for samples obtained from lower aging temperature and higher growing temperature, we relied on heating rates available via our oven (approximately 5 ^oC/min). The resulting white solid products were collected by centrifugation, washed with DI water three times and dried at 50 °C overnight. For convenience, final samples are denoted as GX-Y, where X represents the nucleation aging temperature as above, and Y refers to the subsequent crystal growth temperature.

X-ray diffraction. Phase patterns of the samples were collected with 2θ values ranging

between 5−60° on a Philips X'pert Multi-Purpose diffractometer (MPD) (PANAlytical, Almelo, The Netherlands) operated at 50 kV and 40 mA with Cu Kα radiation (λ=1.5418 Å). Phase identification was via analysis in JADE (9.5.1) with the 2012 PDF4+ database.

Scanning electron microscopy. The morphologies of prepared samples were observed on a Helios NanoLab 600i SEM (FEI, Hillsboro, OR). To ensure good conductivity and imaging, samples were adhered on aluminum stubs that were coated with carbon tape, and then sputter-coated with a ~ 5 nm layer of carbon.

Atomic force microscopy. Low resolution and lattice resolution AFM imaging analyses were carried out on a Dimension Icon AFM (Bruker, USA) in contact mode and a Cypher AFM (Asylim Research, USA) in tapping mode, respectively, to obtain multiscale statistics on the size and thickness of the gibbsite nanoplates. AFM samples were prepared by drop casting gibbsite suspensions that were prepared via dispersing as-synthesized gibbsite nanoparticles into DI water (1mg gibbsite/mL DI water) on silicon wafers, with evaporation assisted by gently flowing nitrogen gas at room temperature.

Nuclear magnetic resonance spectroscopy. A Bruker NMR spectrometer was used at a field strength of 14.0954 T, corresponding to a 156.375 MHz ^{27}Al Larmor frequency, with a MASDVT600W2 BL2.5 X/Y/H probe. To limit sorption of adventitious H_2O, analyzed gibbsites were placed in an ADP-300C vacuum oven (Yamato Scientific), operating at 80 ± 2°C, at a gauge pressure of ca. -100 kPa, overnight. After transfer to an N_2-filled glove box, samples were loaded into a commercial 2.5 mm Bruker rotor, equipped with Vespel drive and bottom caps. Single pulse, direct excitation, ^{27}Al MAS NMR spectra were acquired with ca. 80,000 transients, and an acquisition time of 9.8 ms at a temperature of 25°C. A delay between transients of 0.5 s was used for all samples, sufficient for complete relaxation. Acquisition utilized a single, non-selective, π/20 pulse corresponding to a duration of 0.450 μs at a power level of 50 W (-16.99 dB), determined via a pulse width nutation experiment for a sample of 1 M $Al(H_2O)_6^{3+}$,

prepared via dissolution of aluminum chloride hexahydrate ($AlCl_3 \cdot 6H_2O$, >99%, Sigma-Aldrich) in DI H_2O. Chemical shifts were also referenced to this 1 M $Al(H_2O)_6^{3+}$ solution, where the resonance occurs at 0 ppm. Spectra were collected with a 32 kHz MAS spin rate and processed in Mestrenova (version 14.01-23559, released 2019-06-07, Mestrelab Research S.L.) where the free induction decay was zero-filled to 26 ms and 5 Hz line broadening was applied.

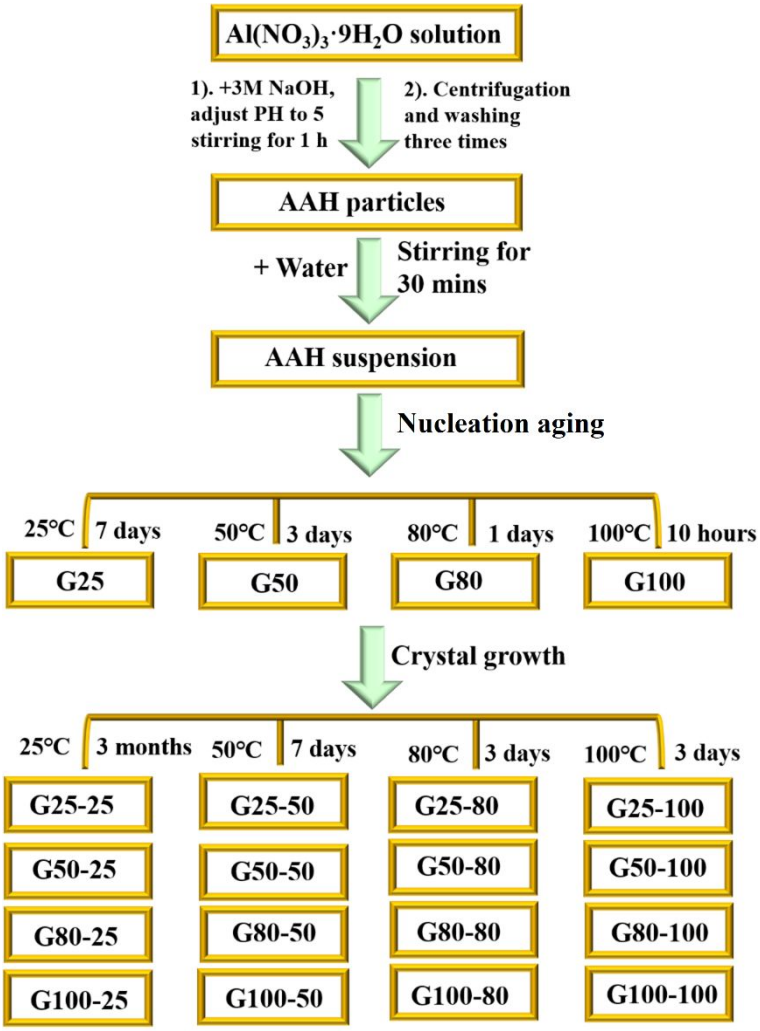

Scheme 1. Flow chart of conditions for two-step gibbsite synthesis used in this study.

Results and Discussion

Effects of separate nucleation aging and crystal growth temperatures on gibbsite properties

Gibbsite nanoplates formed via the two-step route (**Scheme 1**) were characterized by powder XRD, ^{27}Al MAS NMR, SEM, and AFM to validate phase, crystallinity, purity, and morphology, to construct a robust model of particle properties and the probable growth mechanism. An overview of the sample set is given in **Table 1**. XRD patterns in all cases (**Fig. 1**) can be entirely indexed to the standard card of gibbsite (ICDD PDF # 0033-0018), indicating all diffraction peaks belong to monoclinic space group ($P2_{1/n}$) with a= 8.684 Å, b=5.078 Å, c=9.736 Å and β=94.54°.[3, 5, 16] Sharp and strong peaks indicate that the as-prepared gibbsite crystals are highly crystalline. The diffraction peak located at 2θ = 18° is assigned to the (002) facet. XRD also reveals more subtle differences in relative peak strengths in each sample, indicative of anisotropic crystal growth behavior convoluted with some preferential orientation effects.

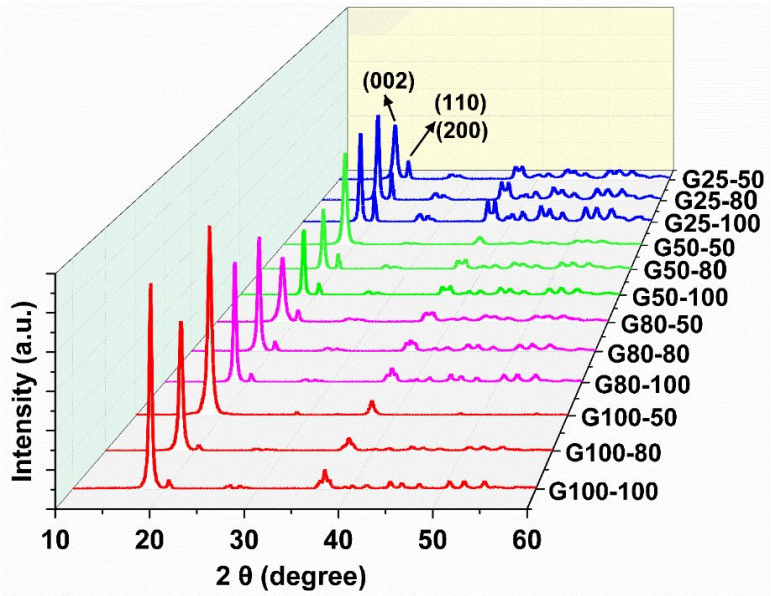

Figure 1. XRD patterns of samples obtained from different nucleation aging and crystal growth temperatures.

^{27}Al MAS NMR was used to assess the defect content of the gibbsite product in terms of undercoordinated Al^{3+} sites (i.e., lower than hexacoordinate). Lower coordinated Al^{3+} species could reflect either residual precursor AAH or undercoordinated sites at crystallite edges, within grain boundaries, dislocations, at oxygen vacancies, etc. This NMR technique is uniquely sensitive to these defects, as

the ^{27}Al isotope is highly abundant (100%)[35] and the chemical shift is very sensitive to aluminum coordination with octahedral, pentahedral and tetrahedral coordinated Al^{3+} occurring between 0-20, 20-50, and 50-80 ppm, respectively.[36]

Compared to the tetra and penta-coordinated Al^{3+} in the AAH, the predominantly octahedral coordination expected in gibbsite yields a prominent resonance appearing ca. 9.5 ppm (**Fig. 2**). Our gibbsites have a very small (trace) amount of tetrahedral Al^{3+}, and the chemical shift of the tetrahedral Al^{3+} (60 - 70 ppm) occurs in a region consistent with tetrahedral Al^{3+} bound through oxygens to octahedral Al^{3+}.[37] Although the tetracoordinate Al^{3+} species occurs in trace amounts of under 0.3% abundance, the trend we observed indicates that with lower nucleation aging temperatures the final product gibbsite contains slightly more tetrahedrally coordinated Al^{3+} sites, consistent with a lower gibbsite nucleation rate at lower temperatures. This alone does not, however, enable attribution to bulk structural defects versus a surface residual of the amorphous precursor material.

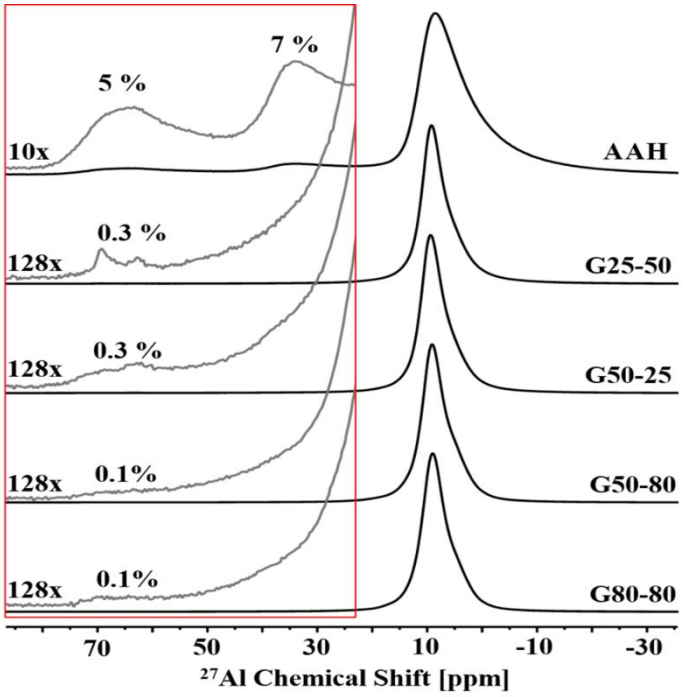

Figure 2. ^{27}Al MAS NMR spectra, at 14.1 T and 32 kHz spinning rate, of the AAH and selected gibbsite samples. Spectra in black are normalized to the same peak height. Vertically offset and magnified spectra are overlaid in gray, with the magnification factor and relative integrated signal intensities of trace Al^{3+} included.

Analysis of the more subtle features in the NMR spectra sheds some light on this aspect. ^{27}Al is a spin 5/2 nuclei, and resonances typically exhibit non-Lorentzian line shapes which are typically defined in terms of quadrupolar coupling parameter, asymmetry parameter and chemical shift (C_Q, η, and δ, respectively). However, for all the gibbsite samples, the resonance appears as a quasi-Lorentzian line shape at 14.1 T, with a weak shoulder apparent around 5 ppm, forming due to the two inequivalent Al^{3+} sites in the crystal structure which exhibit severe overlap in the ^{27}Al MAS NMR spectra at a magnetic field strength of 14.1 T. Compared to literature ^{27}Al MAS NMR spectra of gibbsite at weaker field strengths such as 7.0, 9.4, and 11.7 T,[38-41] acquisition of spectra at 14.1 T in this work and at 20.0 T in previous studies evidently reduces the resolution needed to distinguish between the two symmetry unique octahedral Al^{3+} sites in bulk gibbsite.[5, 13-14, 42] This suggests that resolution of the two gibbsite sites at low field strengths is primarily facilitated by non-equivalent, quadrupolar coupling coefficients of gibbsite (4.6 and 2.2 MHz [38]), while at high field strengths the resolution between the two Al^{3+} sites is limited by their near-identical isotropic chemical shift (13.6 and 11.3 ppm).[38]

Also contributing to the resolution is slight disorder, which in the case of gibbsite would produce a slight distribution of Al^{3+} site parameters.[43] In contrast, the extreme disorder of the AAH manifests in an asymmetrical octahedral Al resonance ca. 8.8 ppm, where the tailing line shape is archetypical of line shapes generated with Czjzek models.[38] These subtle ^{27}Al MAS NMR observations and the more evident lack of penta coordinated Al^{3+} species in gibbsite spectra (which are more abundant than tetra coordinated Al^{3+} species in AAH) suggests that our gibbsite nanoplates entail complete dissolution of the AAH precursor. The observed trace undercoordinated Al^{3+} is therefore more likely to arise from either edge sites or bulk defects in the gibbsite product, and not as a surface residual of the precursor material.

SEM measurements were performed to characterize particle size and morphology, and these findings were complemented by AFM topographic imaging (**Table 1**).

Nanoplates with various edge truncations were obtained depending on the nucleation aging and crystal growth temperatures, ranging from hexagonal, to pseudo-hexagonal, to truncated trigonal, to rhombic shapes (**Fig. 3**). These observed morphologies are inter-related primarily through adjusting the relative growth rates of the two symmetrically inequivalent families of edge terminations along the *a* and *b* crystallographic axes.

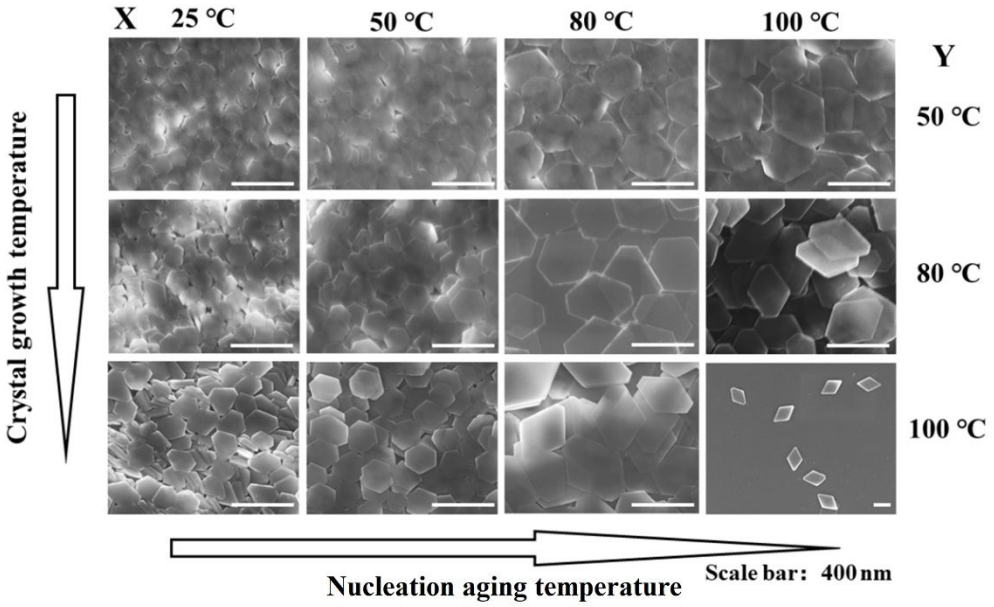

Figure 3. Typical SEM micrographs of gibbsite obtained from different nucleation aging temperatures (X-axis) and crystal growth temperatures (Y-axis). The scale bar in each micrograph corresponds to a length of 400 nm. SEM measurements of gibbsite dimensions are included in **Table 1**.

Table 1. Overview of gibbsite synthesis conditions and characterization results

Entry	Samples	a/nm (SEM)	b/nm (SEM)	a/b	Thickness (c) /nm (AFM)	c/a	c/b
1	G25-50	120±20	130±10	0.92	8±2	0.07	0.06
2	G25-80	140±20	160±10	0.88	10±3	0.07	0.06
3	G25-100	180±30	200±20	0.90	15±5	0.08	0.08
4	G50-50	170±20	200±20	0.85	8±3	0.05	0.04
5	G50-80	180±20	190±30	0.95	10±3	0.06	0.05
6	G50-100	180±20	190±20	0.95	18±5	0.10	0.09
7	G80-50	340±40	350±30	0.97	11±5	0.03	0.03
8	G80-80	420±40	370±40	1.14	13±5	0.03	0.04
9	G80-100	490±50	370±30	1.32	28±5	0.06	0.08
10	G100-50	390±40	370±30	1.05	19±5	0.05	0.05
11	G100-80	500±50	400±50	1.25	37±5	0.07	0.09
12	G100-100	850±50	580±50	1.47	45±5	0.05	0.08

Thickness trends were assessed by AFM topo graphs (**Fig. S2**) with average results compiled in **Table 1.** Predictions from XRD data fitting, where the Debye-Scherrer formula was applied to relate the thickness of gibbsite nanoplates to the full width at half maximum of the (002) diffraction,[16] are given in **Figure S3**. AFM was also used in select cases at high resolution to characterize the nanotopography and atomic order on the basal (001) surfaces. For example, **Figure 4** displays low- and high-resolution AFM images of G50-25 nanoplates, which possess an average size and thickness of 200 nm and 6 nm, respectively. In deflection images, spiral growth features are readily observed (**Fig. 4c**) on the (001) basal surfaces, which suggest screw dislocation based growth in the second step of synthesis.[18, 44] High resolution images at the atomic scale clearly reveal periodic features consistent with a well-ordered lattice that includes the uppermost layers of atoms on the basal surface.

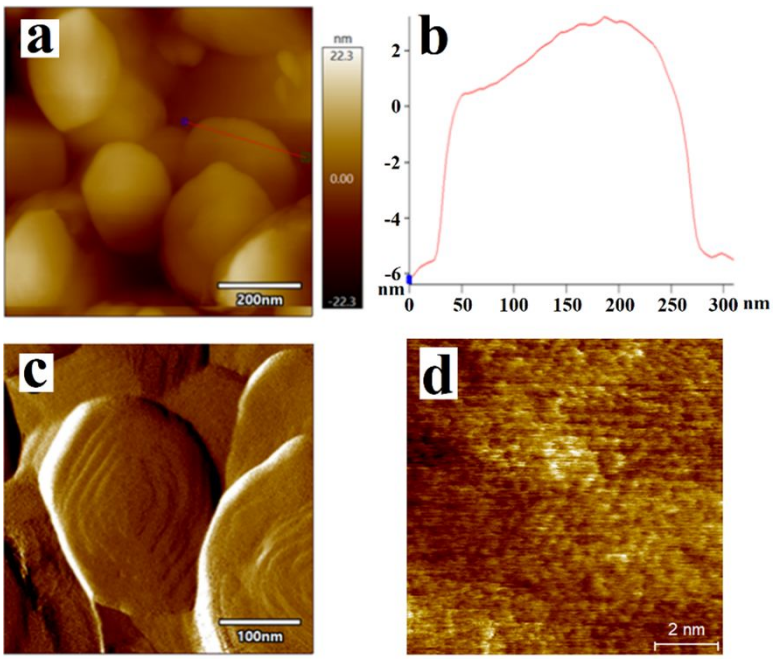

Figure 4. (a) AFM topography image, (b) thickness measurement, (c) deflection error image, and (d) lattice resolution image of the G50-25 nanoplates.

To begin to understand the resulting trends in nanoplatelet growth morphology we focus now on the apparent direction-dependent growth rates that emerge at certain synthesis conditions. Systematic trends apparent in the observed proportions of edge terminations (**Fig. 5**) enabled us to differentiate *a* and *b* crystallographic axes and discuss the results in terms of relative growth rates of crystallographically specific edge faces (**Fig. 5**).

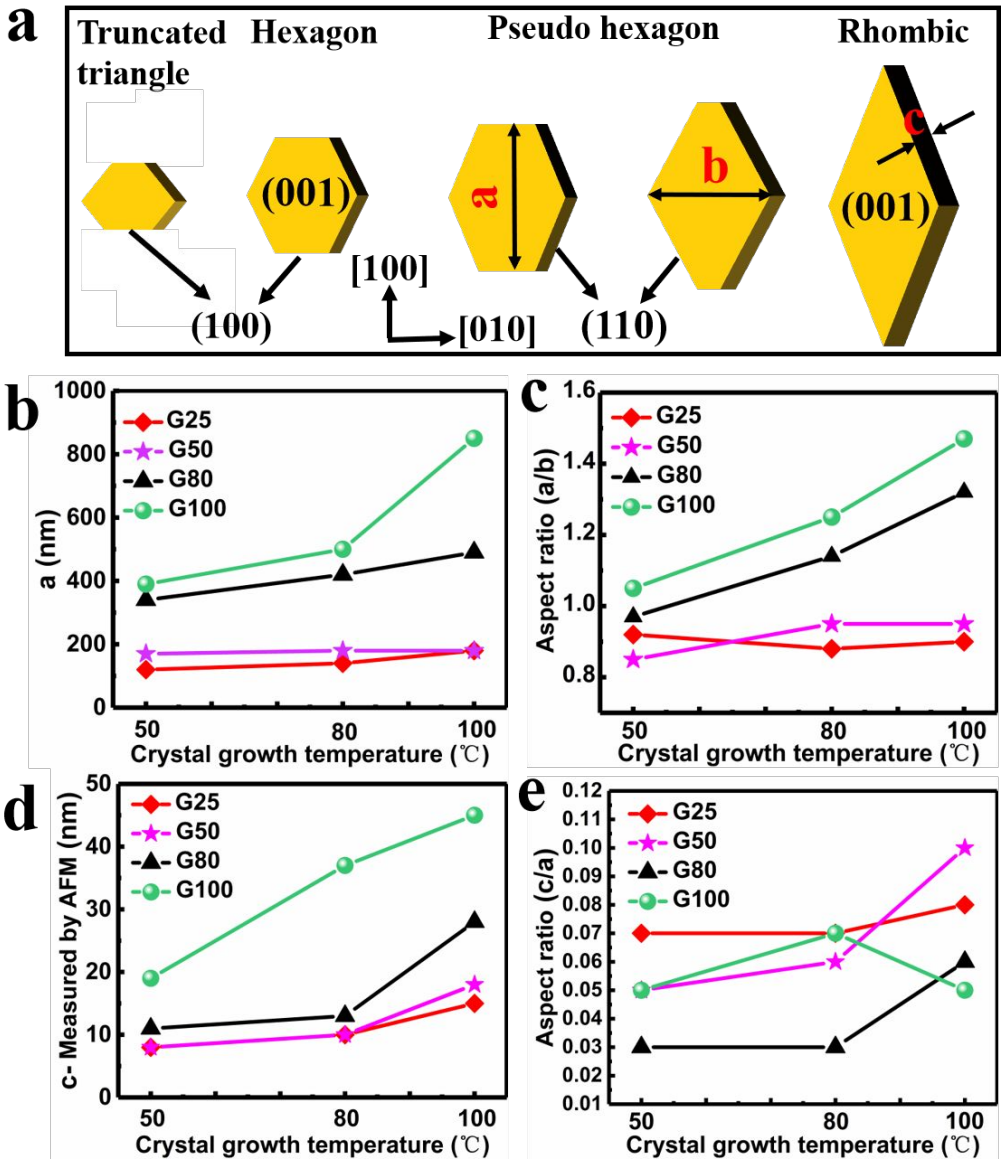

Figure 5. Model of (a) nanoplate morphologies, and data describing the (b) basal plane average diameter, (c) aspect ratio a/b, (d) thickness measured by AFM and (e) aspect ratio c/a. Additional results are shown in **Table 1**.

For AAH suspension aged at 25 and 50°C followed by crystal growth at 50, 80, and 100°C, no significant change in the morphology was detected. The G50-Y series gibbsite nanoplates still present a hexagonal shape, while the shape of the G25-Y series gibbsite nanoplates differed slightly from hexagons to a truncated trigonal shape when the temperature of the crystal growth regime was changed from 50 to 100°C. The ratio of *a* to *b* remained approximately the same for the gibbsite nanoplates obtained from the G50 series, although the G25 series exhibits some dependence, even when the crystal growth temperature is increased to 100°C, indicating there is no apparent

preferential crystal growth along the [100] direction at lower temperature (**Fig. 5c**). Furthermore, there is little dependence between the basal plane diameter of gibbsite nanoplates prepared in the lower nucleation aging temperature solutions (G25 and G50-series), forming 180 nm platelets regardless of crystal growth temperature (**Fig. 5a** and **Table 1**).

In contrast, gibbsite nanoplates obtained after aging the AAH suspension at 80 or 100°C is much faster along the [100] direction compared to other directions perpendicular to [001]. Also, the growth rate along the [010] direction increases upon increasing crystal growth temperature. As shown in **Figure 3**, this results in the formation of the pseudo-hexagonal platelets (evident in G80-80, G80-100, and G100-80) and ultimately leads to the formation of rhombic platelets (G100-100), which is a (100) facet-deficient product. Previous modeling studies indicated the surface energies of gibbsite crystal planes have the order $E_{sur(100)} > E_{sur(110)} > E_{sur(001)}$[45]. In comparation to (001) and (110) planes, the (100) planes are more energetically unstable, and thus the equilibrium morphologies of gibbsite tend to be dominated by two (001) faces with four (110) edges, which agrees well with our experimental observation on the formation of rhombic platelets at high nucleation aging temperature and high crystal growth temperature (**Fig. 3**, G100-100). The ratio of *a* to *b* was found to increase from unity to ca. 1.47 when the crystal growth temperature increased from 50 to 100°C for the G80 and G100 series (**Fig. 5c**). Importantly, AAH suspension aged at 80 to 100°C led to the ability to control the basal plane diameter between 340 nm and 850 nm, respectively, when the crystal growth temperature was increased from 50 to 100°C (yielding size increases of 1.44 and 2.18 times, respectively).

Distinct from the trends of basal plane diameter, the thickness of the gibbsite nanoplates obtained from all different aging solutions generally increased with crystal growth temperature (**Fig. 5d, S2, S3** and **Table 1**), with overall agreement in this trend between AFM and XRD. According to AFM measurements, nanoplatelet thicknesses obtained from G25, G50, G80, and G100 series respectively changed from around 8, 8,

11, and 19 nm to 20, 18, 28, and 45 nm, equating to increases of 2.5, 2.25, 2.55, and 2.84 times when the crystal growth temperature was increased from 50 to 100 °C. The ratio of *c* to *a* (aspect ratio of thickness to particle size) changed from 0.07 to 0.08, 0.05 to 0.10, and 0.03 to 0.06 for nanoplates obtained from the G25, G50 and G80 series, respectively, when the crystal growth temperature was increased from 50 to 100 °C (**Fig. 5b-5e,** and **Table 1**). However, there was no significant changes in the ratio of *c* to *a* for nanoplates obtained from the G100 series. Although there is no preferred growth direction perpendicular to [001] in the G25 and G50 series with increasing crystal growth temperature, growth along the [001] direction increases faster than other directions.

The collective findings demonstrate compositionally pure, gibbsite nanoplates exhibiting tunable morphologies from hexagon, pseudo hexagon, truncated trigonal to rhombic, with diameters from 120 to 850 nm and thickness from 8 to 45 nm. The critical advance was made by simple independent selection of the nucleation aging and crystal growth temperatures. Additionally, gibbsite nanoplates with the same size but of different thickness could be prepared via the lower temperature aging series.

Nucleation and crystal growth mechanism

The observed nucleation and growth behavior appears to follow the concepts embodied in the classical LaMer mechanism,[46-47] which unifies processes leading to the formation and growth of clusters, stable nuclei, and well-defined crystals.[48] Accordingly, three main stages can be defined: (i) the concentration of solvated Al^{3+} precursor species in the solution increases until exceeding a critical supersaturation concentration (C_{crit}); (ii) sufficient agglomeration of these species yields rapid "burst" nucleation; (iii) the concentration of the solvated species sharply decreases thus ending the nucleation process. This finite number of nuclei then grow through addition of remaining Al^{3+} species in solution.

The dissolution rate of the AAH precursor is significantly dependent on the nucleation aging temperatures. At elevated nucleation aging temperatures, the critical

supersaturation level is rapidly reached but only briefly sustained, due to fast consumption of Al^{3+} species, reducing the concentration to levels below the critical value soon after. This results in the remaining Al^{3+} species being distributed between fewer nuclei, forming larger nanoparticles. However, at lower nucleation aging temperatures, a greater number of nuclei form in solution, as the critical concentration is maintained over a longer period of time. This is because the reactivity of the aluminum species in solution is reduced at elevated temperature, leading to more nuclei forming. After the nucleation events subside due to reduction in concentration to below the critical value, the final particle size of gibbsite nanoplates is proportional to the amount of the Al^{3+} remaining in solution.

Furthermore, that the resulting particle sizes depend on the nucleation aging temperature can rationalized based on classical LaMer theory, which asserts that smaller and more equally sized particles arise from higher nucleation rates. As the aging temperature is lowered, two effects are in competition. First is that the solubility with respect to gibbsite decreases. This increases the supersaturation state, which tends to increase the nucleation rate and produce particles with a narrower size distribution.[49] Conversely, the lower reaction temperature can also be expected to reduce the precursor growth rate in the solution, lengthening the induction period for nucleation and thereby yielding a broader size distribution of nanoparticles.[50] As shown in the **Table 1**, in our experiments the gibbsite nanoplates synthesized using a lower nucleation aging temperature always resulted in a broader size distribution. For example, the gibbsite nanoplates G25-50 and G50-50, which synthesized using the 25 ^{o}C or 50 ^{o}C aging solution at 50 ^{o}C for 7 days, respectively, have a size 120 nm with 16.67% size distribution or 170 nm with 11.76% size distribution, respectively; however, the gibbsite nanoplates G80-50 and G100-50, which synthesized using the 80 ^{o}C or 100 ^{o}C aging solution at 50 ^{o}C for 7 days, respectively, have a size 340 nm with 11.76% size distribution or 390 nm with 10.26% size distribution, respectively. Hence, it appears that the increase in supersaturation state with decreasing aging temperature has less of

an impact on nanoparticle outcomes than the corresponding increase in the nucleation time. Varying the nucleation aging temperature was therefore a useful route for controlling the size of the gibbsite nanoplates, consistent with the classical LaMer theory. An illustration of the suggested nucleation and crystallization mechanism is shown in the **Scheme 2**.

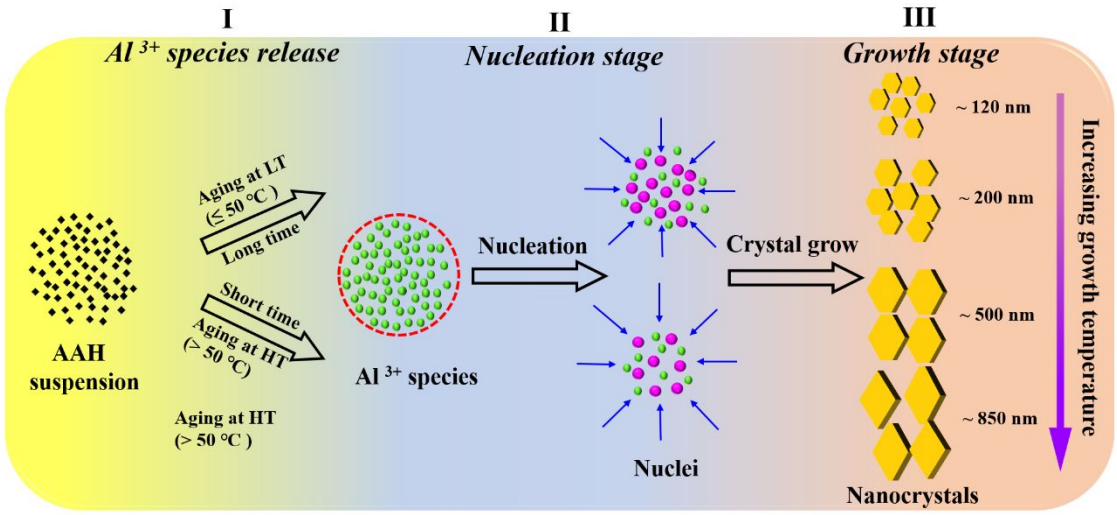

Scheme 2. Illustration of the suggested gibbsite nucleation and crystallization process.

Scale-up production of gibbsite

Given that gibbsite is an important industrial raw material and precursor to produce various alumina products, performing scale-up experiments was valuable to test the possibility of application of this newly developed approach to industry. The above lab-scale results indicate that smaller sized gibbsite nanoplates are obtained in short periods using low temperatures in the nucleation aging step and higher temperatures in the crystal growth step. For instance, gibbsite nanoplates with a basal diameter of ca. 190 nm and a thickness of ca. 10 nm are prepared using 50 ℃ as the nucleation aging temperature for 3 days and 80 ℃ as the crystal growth temperature over another 3 days. A triplicate of 2 L scale-up experiments were performed using similar conditions, 50 and 80 ℃, as the regime aging temperature and crystal growth temperature, respectively, but with the nucleation aging time truncated to 12 h.

As shown in **Figure 6a**, the AAH suspension was heated to 50 ℃ under continuous

stirring for 12 h until all solids disappeared. After further reaction at 80℃ over 3 days, the final product was harvested and characterized. As shown in **Figure 6b**, the XRD result indicated the product is pure gibbsite. Similar as the sample G50-80, the as-synthetic LG50-80 gibbsite nanoplates exhibit hexagonal morphology with an average size ca. 220 nm (**Fig. 6c**). Three scale-up experiments were carried out and the average yield of gibbsite was about 55%. Compared to existing techniques,[30, 33-34] this improved two-step route gibbsite synthesis is cheaper, more efficient and thereby environmentally friendly, providing a scalable methodology to produce gibbsite nanoplates.

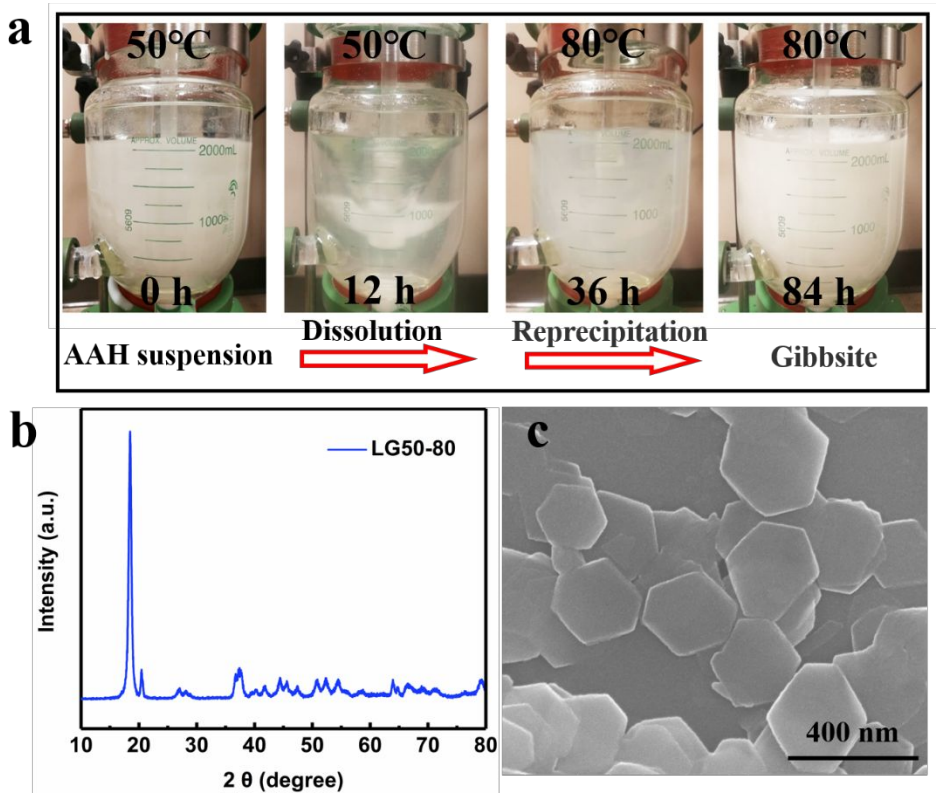

Figure 6. (a) Photographs of the large-scale reaction process (b) XRD pattern and (c) SEM micrographs of the LG50-80 sample.

Conclusions

We have successfully developed an additive free, two-step route to size and morphology-controlled synthesis of gibbsite nanoplatelets using AAH as a precursor. Independent temperature manipulation of the nucleation aging and the crystal growth regimes was used to control the efficacy and yield of the process. Gibbsite nanoplates

with tunable morphologies were produced, ranging in morphology from hexagonal, pseudo-hexagonal, truncated trigonal to rhombohedral, with sizes ranging from 120 to 850 nm, and with thicknesses ranging from 8 to 45 nm. Compared to typical results obtained in prior work, the as-synthetized gibbsite is free of contamination by organics and highly-crystalline. The nucleation aging temperature was found to be the most important factor to control the final particle size of gibbsite nanoplates, with smaller sized gibbsite obtained rapidly using lower temperatures in the nucleation aging step and higher temperatures in the crystal growth step. A series of 2 L scale-up experiments performed to prepare gibbsite nanoplates of 220 nm in size gave an average yield of around 55%, suggesting potential scale-up for industrial purposes. This procedure is not only cheaper, more efficient and environmentally friendlier, but also presents opportunities for manipulation of both primary particle size and facet abundance.

ASSOCIATED CONTENT

Supporting Information

The crystal structure of gibbsite; Topographic AFM image and corresponding cross-section for the as-prepared gibbsite nanoplates; Thickness of as-prepared gibbsite samples determined by XRD fitting; SEM micrographs of GX-25 series gibbsite nanoplates.

AUTHOR INFORMATION

Corresponding Authors

* Email: xin.zhang@pnnl.gov (X. Z.), superfine_jw@126.com (W. J.), and kevin.rosso@pnnl.gov (K. M. R.)

ORCID

Xin Zhang: 0000-0003-2000-858X

Zheming Wang: 0000-0002-1986-4357

Kevin Rosso: 0000-0002-8474-7720

Notes

The authors declare no competing financial interest.

ACKNOWLEDGMENTS

The authors thank Prof. James J. De Yoreo for valuable input regarding the crystal growth mechanism. This research was supported by IDREAM (Interfacial Dynamics in Radioactive Environments and Materials), an Energy Frontier Research Center funded by the U.S. Department of Energy (DOE), Office of Science, Basic Energy Sciences (BES). A portion of this research was performed using EMSL, a national scientific user facility sponsored by the DOE Office of Biological and Environmental Research and located at PNNL. PNNL is a multiprogram national laboratory operated for DOE by Battelle Memorial Institute under Contract DE-AC05-76RL0-1830. SYW acknowledges support from the China Scholarship Council (CSC).

References:

1. Liu, Y.; Ma, D.; Blackley, R. A.; Zhou, W.; Han, X.; Bao, X., Synthesis and Characterization of Gibbsite Nanostructures. *J. Phys. Chem. C* **2008,** *112* (11), 4124-4128.
2. Prange, M. P.; Zhang, X.; Ilton, E. S.; Kovarik, L.; Engelhard, M. H.; Kerisit, S. N., Electronic response of aluminum-bearing minerals. *J. Chem. Phys.* **2018,** *149* (2), 024502.
3. Shen, S.; Chow, P. S.; Chen, F.; Feng, S.; Tan, R. B. H., Synthesis of submicron gibbsite platelets by organic-free hydrothermal crystallization process. *J. Cryst. Growth* **2006,** *292* (1), 136-142.
4. Wijnhoven, J. E., Seeded growth of monodisperse gibbsite platelets to adjustable sizes. *J. Colloid Interface Sci.* **2005,** *292* (2), 403-409.
5. Zhang, X.; Huestis, P. L.; Pearce, C. I.; Hu, J. Z.; Page, K.; Anovitz, L. M.; Aleksandrov, A. B.; Prange, M. P.; Kerisit, S.; Bowden, M. E.; Cui, W.; Wang, Z.; Jaegers, N. R.; Graham, T. R.; Dembowski, M.; Wang, H.-W.; Liu, J.; N'Diaye, A. T.; Bleuel, M.; Mildner, D. F. R.; Orlando, T. M.; Kimmel, G. A.; La Verne, J. A.; Clark, S. B.; Rosso, K. M., Boehmite and Gibbsite Nanoplates for the Synthesis of Advanced Alumina Products. *ACS Appl. Nano Mater.* **2018,** *1* (12), 7115-7128.
6. Freij, S. J.; Parkinson, G. M.; Reyhani, M. M., Atomic force microscopy study of the growth mechanism of gibbsite crystals. *Phy. Chem. Chem.Phys.* **2004,** *6* (5), 1049-1055.
7. Souza, A. D. V.; Arruda, C. C.; Fernandes, L.; Antunes, M. L. P.; Kiyohara, P. K.;

Salomão, R., Characterization of aluminum hydroxide ($Al(OH)_3$) for use as a porogenic agent in castable ceramics. *J. Eur. Ceram. Soc.* **2015,** *35* (2), 803-812.
8. Park, N.-K.; Choi, H.-Y.; Kim, D.-H.; Lee, T. J.; Kang, M.; Lee, W. G.; Kim, H. D.; Park, J. W., Purification of $Al(OH)_3$ synthesized by Bayer process for preparation of high purity alumina as sapphire raw material. *J. Cryst. Growth* **2013,** *373*, 88-91.
9. Reynolds, J. G.; Cooke, G. A.; Herting, D. L.; Warrant, R. W., Evidence for dawsonite in Hanford high-level nuclear waste tanks. *J Hazard Mater* **2012,** *209-210*, 186-92.
10. Huestis, P.; Pearce, C. I.; Zhang, X.; N'Diaye, A. T.; Rosso, K. M.; LaVerne, J. A., Radiolytic stability of gibbsite and boehmite with adsorbed water. *J. Nucl. Mater.* **2018,** *501*, 224-233.
11. Anovitz, L. M.; Zhang, X.; Soltis, J. A.; Nakouzi, E.; Krzysko, A. J.; Chun, J.; Schenter, G. K.; Graham, T. R.; Rosso, K. M.; De Yoreo, J. J.; Stack, A. G.; Bleuel, M.; Gagnon, C.; Mildner, D. F. R.; Ilavsky, J.; Kuzmenko, I., Effects of Ionic Strength, Salt, and pH on Aggregation of Boehmite Nanocrystals: Tumbler Small-Angle Neutron and X-ray Scattering and Imaging Analysis. *Langmuir* **2018,** *34*, 15839−15853.
12. Page, J. S.; Reynolds, J. G.; Cooke, G. A.; Wells, B. E., Large cemented gibbsite agglomerates in alkaline nuclear waste at the Hanford site and the impacts to remediation. *J. Hazard. Mater.* **2019**, 121318.
13. Zhang, X.; Cui, W.; Hu, J. Z.; Wang, H.-W.; Prange, M. P.; Wan, C.; Jaegers, N. R.; Zong, M.; Zhang, H.; Pearce, C. I.; Li, P.; Wang, Z.; Clark, S. B.; Rosso, K. M., Transformation of Gibbsite to Boehmite in Caustic Aqueous Solution at Hydrothermal Conditions. *Cryst. Growth Des.* **2019,** *19* (10), 5557-5567.
14. Graham, T. R.; Hu, J. Z.; Zhang, X.; Dembowski, M.; Jaegers, N. R.; Wan, C.; Bowden, M.; Lipton, A. S.; Felmy, A. R.; Clark, S. B.; Rosso, K. M.; Pearce, C. I., Unraveling Gibbsite Transformation Pathways into LiAl-LDH in Concentrated Lithium Hydroxide. *Inorg. Chem.* **2019,** *58* (18), 12385-12394.
15. Peterson, R. A.; Buck, E. C.; Chun, J.; Daniel, R. C.; Herting, D. L.; Ilton, E. S.; Lumetta, G. J.; Clark, S. B., Review of the Scientific Understanding of Radioactive Waste at the U.S. DOE Hanford Site. *Environ Sci Technol* **2018,** *52* (2), 381-396.
16. Zhang, X.; Zhang, X.; Graham, T. R.; Pearce, C. I.; Mehdi, B. L.; N'Diaye, A. T.; Kerisit, S.; Browning, N. D.; Clark, S. B.; Rosso, K. M., Fast Synthesis of Gibbsite Nanoplates and Process Optimization using Box-Behnken Experimental Design. *Cryst. Growth Des.* **2017,** *17* (12), 6801-6808.
17. Andrew R. Hind, S. K. B., Stephen C. Grocott. The surface chemistry of Bayer process solids: a review. *Colloid Surface A.* **1999,** 146 (1-3), 359–374.
18. Freij, S. J.; Parkinson, G. M., Surface morphology and crystal growth mechanism of gibbsite in industrial Bayer liquors. *Hydrometallurgy* **2005,** *78* (3-4), 246-255.
19. Freij, S. J.; Parkinson, G. M.; Reyhani, M. M., Direct observation of the growth of gibbsite crystals by atomic force microscopy. *J. Cryst. Growth* **2004,** *260* (1-2), 232-242.
20. Bai, F.; Bian, K.; Huang, X.; Wang, Z.; Fan, H., Pressure Induced Nanoparticle

Phase Behavior, Property, and Applications. *Chem. Rev.* **2019,** *119* (12), 7673-7717.
21. Bian, K.; Li, R.; Fan, H., Controlled Self-Assembly and Tuning of Large PbS Nanoparticle Supercrystals. *Chem. Mater.* **2018,** *30* (19), 6788-6793.
22. Wang, Z.; Bian, K.; Nagaoka, Y.; Fan, H.; Cao, Y. C., Regulating Multiple Variables To Understand the Nucleation and Growth and Transformation of PbS Nanocrystal Superlattices. *J. Am. Chem. Soc.* **2017,** *139* (41), 14476-14482.
23. Dunphy, D.; Fan, H.; Li, X.; Wang, J.; Brinker, C. J., Dynamic investigation of gold nanocrystal assembly using in situ grazing-incidence small-angle X-ray scattering. *Langmuir* **2008,** *24* (19), 10575-10578.
24. Liu, L.; Zhang, S.; Bowden, M. E.; Chaudhuri, J.; Yoreo, J. J. D., In Situ TEM and AFM Investigation of Morphological Controls during the Growth of Single Crystal BaWO4. *Cryst. Growth Des.* **2017,** *18* (3), 1367-1375.
25. Yan, F.; Liu, L.; Walsh, T. R.; Gong, Y.; El-Khoury, P. Z.; Zhang, Y.; Zhu, Z.; De Yoreo, J. J.; Engelhard, M. H.; Zhang, X.; Chen, C. L., Controlled synthesis of highly-branched plasmonic gold nanoparticles through peptoid engineering. *Nat. Commun.* **2018,** *9* (1), 2327.
26. Zong, M.; Zhang, X.; Wang, Y.; Huang, X.; Zhou, J.; Wang, Z.; De Yoreo, J. J.; Lu, X.; Rosso, K. M., Synthesis of 2D Hexagonal Hematite Nanosheets and the Crystal Growth Mechanism. *Inorg. Chem.* **2019,** *58* (24), 16727-16735.
27. Liu, L.; Sushko, M. L.; Buck, E. C.; Zhang, X.; Kovarik, L.; Shen, Z.; Tao, J.; Nakouzi, E.; Liu, J.; De Yoreo, J. J., Revisiting the Growth Mechanism of Hierarchical Semiconductor Nanostructures: The Role of Secondary Nucleation in Branch Formation. *J. Phys. Chem. Lett.* **2019,** *10* (21), 6827-6834.
28. Huang, X.; Hou, X.; Zhang, X.; Rosso, K. M.; Zhang, L., Facet-dependent contaminant removal properties of hematite nanocrystals and their environmental implications. *Environ. Sci. Nano* **2018,** *5* (8), 1790-1806.
29. Zhang, X.; Cui, W.; Page, K. L.; Pearce, C. I.; Bowden, M. E.; Graham, T. R.; Shen, Z.; Li, P.; Wang, Z.; Kerisit, S.; N'Diaye, A. T.; Clark, S. B.; Rosso, K. M., Size and Morphology Controlled Synthesis of Boehmite Nanoplates and Crystal Growth Mechanisms. *Cryst. Growth Des.* **2018,** *18* (6), 3596-3606.
30. Louaer, S.; Wang, Y.; Guo, L., Fast synthesis and size control of gibbsite nanoplatelets, their pseudomorphic dehydroxylation, and efficient dye adsorption. *ACS Appl. Mater. Interfaces* **2013,** *5* (19), 9648-9655.
31. May, M.; Navarrete, J.; Asomoza, M.; Gomez, R., Tailored mesoporous alumina prepared from different aluminum alkoxide precursors. *J. Porous Mater.* **2007,** *14* (2), 159-164.
32. Judith E. G. J. Wijnhoven, D. l. D. v. t. Z., David van der Beek, and Henk N. W. Lekkerkerker*, Sedimentation and Phase Transitions of Colloidal Gibbsite Platelets. *Langmuir* **2005,** *21*, 10422-10427.
33. Rosenqvist, J.; Persson, P.; Sjöberg, S., Protonation and charging of nanosized gibbsite (α-Al (OH) 3) particles in aqueous suspension. *Langmuir* **2002,** *18* (12), 4598-4604.

34. Kumara, C. K.; Ng, W. J.; Bandara, A.; Weerasooriya, R., Nanogibbsite: synthesis and characterization. *J. Colloid Interface Sci.* **2010,** *352* (2), 252-8.
35. Akitt, J. W., Multinuclear studies of aluminium compounds. *Prog. Nucl. Magn. Reson. Spectrosc.* **1989,** *21* (1-2), 1-149.
36. Haouas, M.; Taulelle, F.; Martineau, C., Recent advances in application of (27)Al NMR spectroscopy to materials science. *Prog. Nucl. Magn. Reson. Spectrosc.* **2016,** *94-95*, 11-36.
37. Müller, D.; Gessner, W.; Samoson, A.; Lippmaa, E.; Scheler, G., Solid-state aluminium-27 nuclear magnetic resonance chemical shift and quadrupole coupling data for condensed AlO_4 tetrahedra. *J. Chem. Soc., Dalton Trans.* **1986,** *6*, 1277-1281.
38. Chandran, C. V.; Kirschhock, C. E. A.; Radhakrishnan, S.; Taulelle, F.; Martens, J. A.; Breynaert, E., Alumina: discriminative analysis using 3D correlation of solid-state NMR parameters. *Chem. Soc. Rev.* **2019,** *48* (1), 134-156.
39. Chen, L.; Ye, G.; Xu, D.; Zhu, L.; Lu, Z.; Dong, L.; Liu, Y., Chemical bond change of gibbsite and fumed silica mixture during mechanical activation. *Mater.Lett.* **2012,** *85*, 91-94.
40. Graham, T. R.; Dembowski, M.; Martinez-Baez, E.; Zhang, X.; Jaegers, N. R.; Hu, J.; Gruszkiewicz, M. S.; Wang, H. W.; Stack, A. G.; Bowden, M. E.; Delegard, C. H.; Schenter, G. K.; Clark, A. E.; Clark, S. B.; Felmy, A. R.; Rosso, K. M.; Pearce, C. I., In Situ (27)Al NMR Spectroscopy of Aluminate in Sodium Hydroxide Solutions above and below Saturation with Respect to Gibbsite. *Inorg. Chem.* **2018,** *57* (19), 11864-11873.
41. Malki, A.; Mekhalif, Z.; Detriche, S.; Fonder, G.; Boumaza, A.; Djelloul, A., Calcination products of gibbsite studied by X-ray diffraction, XPS and solid-state NMR. *J. Solid State Chem.* **2014,** *215*, 8-15.
42. Hu, J. Z.; Zhang, X.; Jaegers, N. R.; Wan, C.; Graham, T. R.; Hu, M.; Pearce, C. I.; Felmy, A. R.; Clark, S. B.; Rosso, K. M., Transitions in Al Coordination during Gibbsite Crystallization Using High-Field ^{27}Al and ^{23}Na MAS NMR Spectroscopy. *The Journal of Physical Chemistry C* **2017,** *121* (49), 27555-27562.
43. Ashbrook, S. E.; McManus, J.; MacKenzie, K. J.; Wimperis, S., Multiple-quantum and cross-polarized ^{27}Al MAS NMR of mechanically treated mixtures of kaolinite and gibbsite. *J. Phys. Chem. B* **2000,** *104* (27), 6408-6416.
44. Sonthalia, R.; Behara, P.; Kumaresan, T.; Thakre, S., Review on alumina trihydrate precipitation mechanisms and effect of Bayer impurities on hydrate particle growth rate. *Int. J. Miner. Process* **2013,** *125*, 137-148.
45. Liu, G.-h.; Li, Z.; Li, X.-b.; Qi, T.-g.; Peng, Z.-h.; Zhou, Q.-s., Precipitation of spherical boehmite from concentrated sodium aluminate solution by adding gibbsite as seed. Int. J. Min. Met. Mater. 2017, 24 (8), 954-963.
46. Thanh, N. T.; Maclean, N.; Mahiddine, S., Mechanisms of nucleation and growth of nanoparticles in solution. *Chem. Rev.* **2014,** *114* (15), 7610-30.
47. Chu, D. B. K.; Owen, J. S.; Peters, B., Nucleation and Growth Kinetics from LaMer Burst Data. *J. Phys. Chem. A* **2017,** *121* (40), 7511-7517.

48. Xiong, Y.; Xia, Y., Shape-Controlled Synthesis of Metal Nanostructures: The Case of Palladium. *Adv. Mater.* **2007,** *19* (20), 3385-3391.
49. Oskam, G., Metal oxide nanoparticles: synthesis, characterization and application. *J. Solgel. Sci. Technol.* **2006,** 37(3), 161-164.
50. Wu, Z.; Yang, S; Wu, W.,. Shape control of inorganic nanoparticles from solution. *Nanoscale*, **2016**, 8(3), 1237-1259.

Graphical Abstract

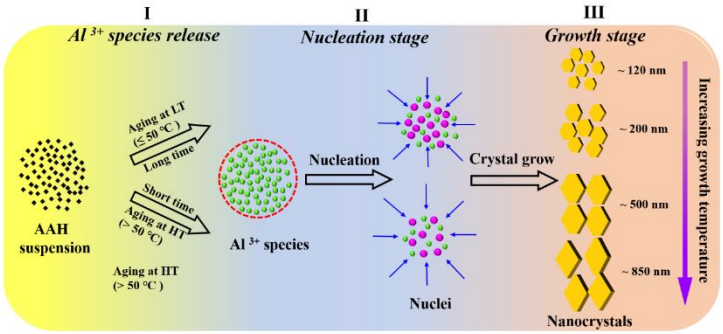

Size and shape-controlled synthesis of gibbsite nanoplates via an additive-free two-step route.